Chinese Chemical Letters 32 (2021) 649–659

Contents lists available at ScienceDirect

Chinese Chemical Letters

journal homepage: www.elsevier.com/locate/cclet

Review

Applications of metal–organic framework composites in CO_2 capture and conversion

Jiewei Liu[a,b,d], Chunying Chen[c], Kun Zhang[a], Li Zhang[c,*]

[a] School of Biotechnology and Health Sciences, Wuyi University, Jiangmen 529020, China
[b] International Healthcare Innovation Institute (Jiangmen), Jiangmen 529040, China
[c] School of Chemistry, Sun Yat-sen University, Guangzhou 510275, China
[d] School of Chemical Engineering and Light Industry, Guangdong University of Technology, Guangzhou 510006, China

ARTICLE INFO

Article history:
Received 9 June 2020
Received in revised form 6 July 2020
Accepted 24 July 2020
Available online 25 July 2020

Keywords:
Metal-organic framework composites
CO_2 chemical fixation
CO_2 hydrogenation
CO_2 photoreduction
CO_2 electroreduction
CO_2 photoelectroreduction

ABSTRACT

Reliable technologies for CO_2 capture and conversion (C3) are of vital importance for the establishment of a sustainable society. Metal-organic framework (MOF) composites have shown their compelling potentials for C3 due to the plentiful reticular chemistry of MOF structures and the synergistic catalysis between MOFs and the functional guests. This review focuses on the syntheses and catalytic applications towards C3 of MOF composites, which is divided into three sections. The first section gives a brief introduction about synthetic strategies of MOF composites. The second section discusses the recent progress of MOF composites in C3, including CO_2 chemical fixation, hydrogenation, photoreduction, electroreduction and photoelectroreduction. The third section summarizes the challenges and future prospects of MOF composites for C3. We hope that this review cannot only provide an inspiration for the rational design of MOF composites for C3, but also stimulate more and more research works in this emerging area.

1. Introduction

The burning of fossil fuels contributes to a major CO_2 emission to our planet. The anthropogenic CO_2 discharge outpaces the natural carbon cycle in natural environment, leading to current global climate changes and adverse impact on humankinds. To establish a sustainable society, reliable technologies for CO_2 capture and conversion (C3) are certainly important and imperative [1–6]. CO_2 can be converted into valuable chemicals through chemical fixation [7], hydrogenation [8], photocatalysis [9], electrocatalysis [10] and photoelectrocatalysis [11]. However, the efficient CO_2 conversion is hampered by the high chemical stability of the C=O bond (bond enthalpy, 805 kJ/mol), which requires a high energy input for bond cleavage [12]. Therefore, efficient catalysts that can capture and activate the inert CO_2 molecules are highly desirable.

Various kinds of porous materials have been investigated for the C3, including ionic liquids (ILs), zeolites, porous carbons, porous organic polymers, covalent organic frameworks (COFs) and metal–organic frameworks (MOFs). Among them, MOFs are promising candidates for C3 application due to their high porosity, surface areas, structural diversity and functional adjustability [13–16].

The plentiful reticular chemistry of MOF structures offers opportunities for the rational design of MOF composites [17,18].

Firstly, the cavities of MOFs can be used for CO_2 adsorption. In addition, a range of functional materials such as homogeneous catalysts, semiconductors, metal nanoparticles (MNPs) and quantum dots (QDs), which are beneficial for CO_2 activation, can be immobilized into MOFs, giving rise to MOF composites. Moreover, the definite and uniform structures of MOFs will benefit the study of the interactions between CO_2 and frameworks at a molecular level. Last but not the least, synergistic effect between MOFs and the functional materials can effectively improve the catalytic performances of MOFs composites. With the integration of MOF and functional materials, the MOF composites combine their merits: on one hand, the MOFs possess high porosity and tailorable structure, and on the other hand, the functional materials have excellent catalytic, optical or electrical properties, and therefore they can display enhanced activity, selectivity, and stability in the catalytic applications (Fig. 1).

This review focuses on the syntheses and catalytic applications towards C3 of MOF composites, which is divided into three sections. The first section gives a brief introduction about the

* Corresponding author.
E-mail address: zhli99@mail.sysu.edu.cn (L. Zhang).

https://doi.org/10.1016/j.cclet.2020.07.040
1001-8417/

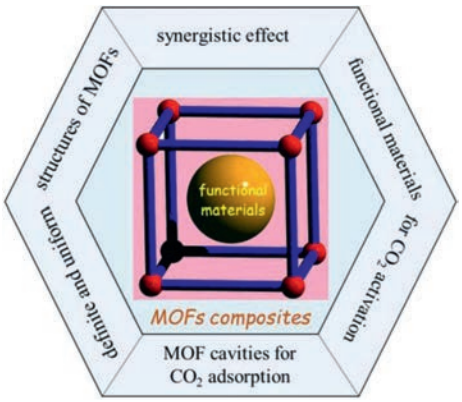

Fig. 1. The advantages of MOF composites for the CO_2 capture and conversion.

synthetic strategies of MOF composites. The second section discusses the recent progress of MOF composites in C3, including CO_2 chemical fixation, hydrogenation, photoreduction, electroreduction and photoelectroreduction. The third section summarizes the challenges and future prospects of MOF composites for C3.

2. Synthetic strategies of metal–organic framework composites

In general, the preparation of MOF composites is achieved either *via* the encapsulation of functional materials in the pores or layers of MOFs or coating MOFs with functional supports/layers [17–20]. According to the different types of functional materials, MOF composites that were used for C3 application can be classified into four types as following:

(1) MNPs@MOFs. There were three methods for the preparation of MNPs@MOFs: 1) Ship-in-bottle strategy. The precursors were dispersed inside the pores of MOFs, and followed by the *in situ* formation of the MNPs *via* reduction. 2) Bottle-around-ship strategy. The MNPs were prepared firstly, and then MOFs grew *in situ* on the surfaces of the MNPs. 3) One-pot synthesis. The MNPs and MOFs were formed simultaneously to afford the MNPs@MOFs.
(2) Semiconductor (or QDs)@MOFs. They could be prepared by the ship-in-bottle or bottle-around-ship strategy. The stability of semiconductor or QDs can be improved by the encapsulation into the pores of the MOFs, and meanwhile their size-dependent electronic or optical properties can be maintained.
(3) Homogeneous molecular catalysts@MOFs. They were prepared *via* covalent bonding or non-covalent interactions between the molecular catalysts and MOFs. After the homogeneous molecular catalysts were immobilized into MOFs, not only their catalytic performances remained but also the side reactions such as the oxidative self-degradation could be overcome.
(4) Ionic liquids@MOFs (ILs@MOFs). They could be prepared through tandem postsynthetic modification, capillary action or *in situ* polymerization of ILs inside the MOF pores. After incorporating ILs into MOFs, the resultant ILs@MOFs were formed.

3. Metal-organic framework composites for CO_2 capture and conversion

3.1. Cycloaddition of CO_2 and epoxides

Cycloaddition of CO_2 and epoxides represents one of the few promising industrial processes in which CO_2 can be utilized under mild temperature and pressure. The value-added carbonate products are important chemical intermediates that can be utilized for a variety of fine chemical synthesis and fabrication of functionalized materials. Enhanced activity and selectivity for the coupling reaction of CO_2 and epoxides can be achieved through the encapsulation of functional species within the porous framework [21–25]. As summarized in Table 1, a range of MOF composites for the CO_2 chemical conversion have been reported.

Jiang *et al.* incorporated the imidazolium-based poly(ionic liquid)s (denoted as polyILs) into MIL-101 to prepare the polyILs@MIL-101 *via* the *in situ* polymerization of ILs (Fig. 2) [21]. The composite polyILs@MIL-101 showed a higher isosteric heats of CO_2 adsorption (Q_{st}) value (44 kJ/mol) at zero coverage than that of MIL-101 (26 kJ/mol), indicating that a stronger affinity existed between CO_2 molecules and polyILs@MIL-101. The synergistic effect from the exposed Lewis acid sites (Cr^{3+}) in MIL-101 and the Lewis base sites (Br^-) in polyILs contributed to the activation and subsequent reaction of CO_2 and epoxides. The composite exhibited an excellent catalytic activity toward the cycloaddition of CO_2 and epoxides under mild conditions (1 bar CO_2, $\leq$ 70 °C) in the absence of any cocatalyst (Table 1, entry 1). In addition, polyILs@MIL-101 did not show any drop of the catalytic activity at a CO_2 pressure ranging from 1.5 bar to 0.75 bar, and a decent activity (~80%) can be maintained even under 0.5 bar of CO_2 pressure. PolyILs@MIL-101 can be recycled for 10 runs without a significant loss of activity.

Sun and Ma *et al.* incorporated a linear ionic polymer (IP) into the pores of MIL-101 to afford the IP@MIL-101 [22]. The Lewis acid

Fig. 2. The preparation of polyILs@MIL-101. Reproduced with permission [21]. Copyright 2018, American Chemical Society.

Table 1
Application of MOF composites in the CO_2 chemical conversion.

Entry	MOF composites catalyst	Active site	Base	Substrate	Reaction condition	Yield (%)	Ref.
1	polyILs@MIL-101	Cr^{3+} & Br^-	–	Epichlorohydrin	1 bar, 70 °C, 24 h	94	[21]
2	MIL-101-IP	Cr^{3+} & Br^-	–	Propylene oxide	1 bar, 50 °C, 68 h	99	[22]
3	mesoCu@Al-bpydc	Al^{3+} & bipyridine	–	Propylene oxide	10 bar, 60 °C, 24 h	98.8	[23]
4	Ag@MIL-101	Ag NPs	Cs_2CO_3	1-Ethynylbenzene	1 bar, 50 °C, 15 h	96.5	[28]
5	$Au_{12}Ag_{32}(SR)_{30}$@ZIF-8	$Au_{12}Ag_{32}(SR)_{30}$ nanocluster	K_2CO_3	1-Ethynylbenzene	1 bar, 50 °C, 24 h	100	[29]
6	0.5Ag@ZIF-8	Ag NPs	Cs_2CO_3	1-Ethynylbenzene	1 bar, 40 °C, 20 h	97	[30]

site (Cr^{3+}) within the MIL-101 and the nucleophilicity of the Br^- ions cooperatively interacted to significantly enhance the catalytic performances. IP@MIL-101 exhibited higher conversions (99%) than the individual parts or a physical mixture of both (Table 1, entry 2).

Yang and Chen *et al*. developed an *in situ* defect-formation strategy to obtain the hierarchical mesoCu@Al-bpydc [23]. This composite was constructed by the loading of copper precursor $Cu(BF_4)_2$ into the as-synthesized Al-bpydc *via* a wet-impregnation method (Fig. 3). The defect-mesopore was formed within microporous Al-bpydc. The BF_4^- anion induced the formation of mesopore within Al-bpydc, and the anchored Cu^{2+} ions functioned as Lewis acid catalysts for the CO_2 cycloaddition reaction. Under low pressures ($P/P_0 < 0.2$), mesoCu@Al-bpydc presented a much higher CO_2 sorption capacity than Al-bpydc. Catalytic results showed that mesoCu@Al-bpydc displayed high reactivity and selectivity for the CO_2 cycloaddition reaction with a range of epoxides, which should be attributed to the active Cu^{2+} Lewis acid sites and bipyridine N basic sites as well as the strong affinity of the composite toward CO_2 (Table 1, entry 3). Moreover, the hierarchically structure could further enhance the mass transfer efficiency of the substrate. The mesoCu@Al-bpydc can be recycled for 5 runs without loss of activity.

3.2. Reaction of CO_2 and terminal alkynes

Carboxylation of terminal alkynes is considerably greener over other options for the preparation of propiolic acids, which are important intermediates in chemical and pharmaceutical industries [26,27]. MNPs@MOFs can be used for the carboxylation of terminal alkynes with CO_2 [28–34].

Ma and Cheng *et al*. prepared Ag@MIL-101 using a simple liquid impregnation method, and applied the composite in the reaction of terminal alkynes and CO_2 to prepare propiolic acids [28]. Due to the large pore size (2.9–3.4 nm), high specific surface area and long-term chemical stability, MIL-101 was chosen as the support. TEM images disclosed that Ag NPs with an average size of 1.4 ± 0.4 nm were uniformly dispersed in MIL-101. Catalytic studies showed that under the optimized conditions (1.5 equiv. Cs_2CO_3, 1 bar CO_2, DMF, 50 °C), Ag@MIL-101 could convert the alkyne substrates to the corresponding propiolic acids in excellent yields (Table 1, entry 4). The excellent catalytic activities of Ag@MIL-101 could be explained in three ways: 1) MIL-101 served as CO_2 reservoirs and then increased the local CO_2 concentration around Ag NPs, which were the active sites; 2) The inner cavities of MIL-101 provided a platform for the reaction of CO_2 with terminal alkynes; 3) Ag NPs were stabilized by MIL-101. A plausible reaction mechanism was proposed: Through the windows of MIL-101, the terminal alkynes diffused into the inner cavities and reacted with Ag NPs to generate the silver acetylide intermediates in the presence of Cs_2CO_3. Afterwards, CO_2 inserted into the C-Ag bond to generate the carboxylic acid products.

Using an electrostatic self-assembly strategy, Sheng and Zhu *et al*. incorporated the anionic $[Au_{12}Ag_{32}(SR)_{30}]^{4-}$ into ZIF-8 to obtain the $Au_{12}Ag_{32}(SR)_{30}$@ZIF-8 [29]. The high-angle annular dark field scanning transmission electron microscopy (HAADF-STEM), TEM images as well as energy dispersive X-ray (EDX) element mapping disclosed that the $[Au_{12}Ag_{32}(SR)_{30}]^{4-}$ nanoclusters were uniformly dispersed in the ZIF-8 matrix. Catalytic studies showed that $Au_{12}Ag_{32}(SR)_{30}$@ZIF-8 gave rise to 100% conversion of phenylacetylene into phenylpropiolate under mild conditions (50 °C and ambient CO_2 pressure) (Table 1, entry 5). The turn-over number (TON) was as high as 18164. In addition, the high catalytic activity could be also maintained in five consecutive runs. A possible catalytic mechanism was proposed: The $[Au_{12}Ag_{32}(SR)_{30}]^{4-}$ firstly activated the terminal alkyne with a base to form a $Ph{-}C{\equiv}C\cdots Au_{12}Ag_{32}(SR)_{30}$ intermediate I, and then CO_2 was fixed and activated by ZIF-8 to generate an intermediate CO_2-Lewis acid complex II. Subsequently, the activated CO_2 inserted into the nearby Au–C bond to afford the carboxylate III. Finally, the intermediate I was regenerated by the metathesis with alkyne (Fig. 4).

The different locations of MNPs relative to the MOFs in the composites contributed differently to the reaction efficiency. Sun and Wei *et al*. prepared 0.5Ag@ZIF-8 (where 0.5 represents the Ag/Zn ratio in the preparation mixtures) by rapidly contacting $AgNO_3$ and ZIF-8 in methanol at 0 °C. Two types of Ag species were installed, including the highly dispersed Ag(I) in the backbone (Ag^{HD}) and the aggregated Ag(0) nanoparticles on the outer surface (Ag^{NP}) [30]. Under the optimized condition, 0.5Ag@ZIF-8 promoted the carboxylation of terminal alkynes with CO_2 into the corresponding propiolic acids in good to excellent yields (Table 1, entry 6). The coexistence of Ag^{HD} and Ag^{NP} had a profound effect on the catalytic performances: On one hand, Ag^{NP} were highly effective for the activation of terminal alkynes, and on the other hand, the modification of ZIF-8 framework with Ag^{HD} enhanced its CO_2 affinity and thus improved the CO_2 activation. The 0.5Ag@ZIF-8 can be recycled for 4 runs with a negligible alteration on the crystallinity and morphology.

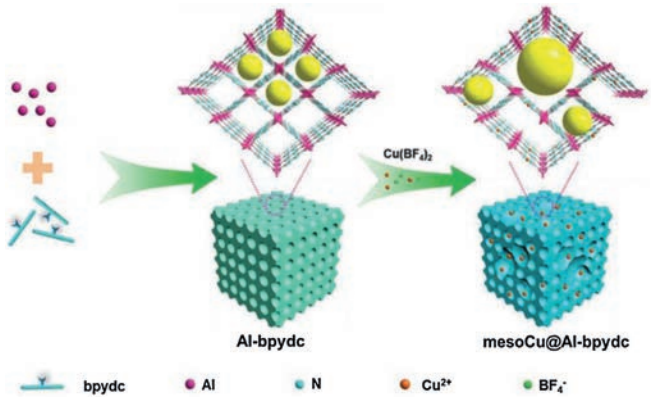

Fig. 3. The synthesis of mesoCu@Al-bpydc. Reproduced with permission [23]. Copyright 2019, Wiley-VCH.

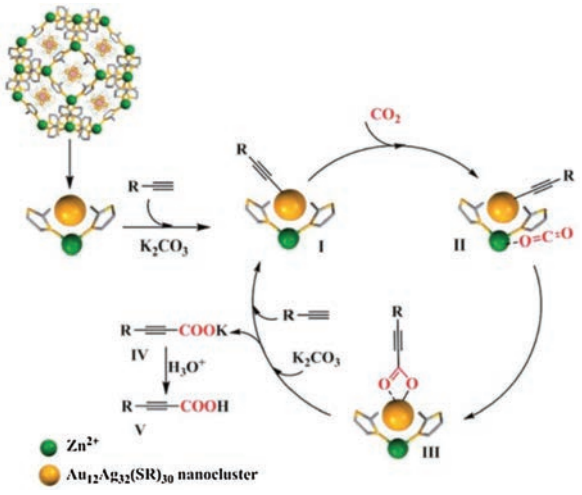

Fig. 4. Proposed reaction mechanism toward CO_2 and phenylacetylene over $Au_{12}Ag_{32}(SR)_{30}$@ZIF-8. Reproduced with permission [29]. Copyright 2018, Royal Society of Chemistry.

Table 2
Application of MOF composites in CO_2 hydrogenation.

Entry	MOF composite	Temperature (°C)	Pressure (bar)	Product	TOF (h^{-1})	Ref.
1	Cu ⊂ UiO-66	175	10 (H_2/CO_2 = 3)	CH_3OH	10	[36]
2	Cu/ZnOx@UiO-bpy	250	40 (H_2/CO_2 = 3)	CH_3OH	2.59 g_{MeOH} kg_{Cu}^{-1} h^{-1}	[37]
3	Au&Pt@ZIF	150	32 (H_2/CO_2 = 3)	CH_3OH	1522	[38]
4	[Ru]@UiO-66	27	15 (H_2/CO_2 = 4)	HCOOH	6×10^5	[39]
5	Ni@MOF-5	280	1 (H_2/CO_2 = 4)	CH_4	75% conversion	[40]
6	20Ni@MIL-101	300	1 (H_2/CO_2 = 4)	CH_4	5.868	[41]
7	Ni@UiO-66	320	10 (H_2/CO_2 = 3)	CH_4	154.8	[42]

3.3. CO_2 hydrogenation

3.3.1. CO_2-to-CH_3OH

CO_2 hydrogenation can not only slow down the rising CO_2 level in Earth's atmosphere, but also produce value-added chemicals such as methanol and formate. The $Cu/ZnO/Al_2O_3$ is used as an industrial catalyst for CO_2 hydrogenation to prepare methanol, but however CO was observed as the byproduct due to the reverse water-gas shift reaction [35].

Yaghi and Somorjai *et al.* reported the synthesis of Cu@UiO-66, which was efficient for CO_2 hydrogenation at 175 °C and 10 bar (CO_2 and H_2 in the 1:3 molar ratio) and produced methanol with 100% selectivity [36] (Table 2, entry 1). The turn-over frequency (TOF) was calculated to be 10 h^{-1}, which was 8 times of that of the benchmark $Cu/ZnO/Al_2O$ catalyst. XPS results disclosed that the Zr 3d binding energy in Cu@UiO-66 was shifted toward lower oxidation state compared to UiO-66, implying that the Zr(IV) was reduced after being in contact with the Cu NPs due to the metal-support interaction effect.

The Cu/ZnO_x interfaces were widely used for CO_2 hydrogenation, but however, Cu NPs slowly aggregated and separated from ZnO_x under the reaction conditions, reducing the Cu/ZnO_x interfaces and thus diminishing the catalytic activity. Wang and Lin *et al.* prepared the Cu/ZnO_x@UiO-bpy (bpy = 2,2′-bipyridine) composite by anchoring the ultrasmall Cu/ZnO_x nanoparticles in the framework of UiO-bpy, which can prevent the agglomeration of Cu NPs and phase separation between Cu and ZnO_x [37]. Cu/ZnO_x@UiO-bpy was prepared by the coordination of the Cu^{2+} ions into the bpy sites that were located in UiO-bpy through the postsynthetic metalation, and followed by the incorporation of Zn^{2+} ions *via* their reactions with the μ_3-OH sites on the Zr-O SBUs of UiO-bpy. The ultrasmall Cu/ZnO_x NPs were then *in situ* generated within UiO-bpy at 250 °C in the presence of H_2 as the reductant, giving rise to Cu/ZnO_x@UiO-bpy. Catalytic studies showed that Cu/ZnO_x@UiO-bpy-catalyzed CO_2 hydrogenation produced methanol with yields up to 2.59 g_{MeOH} kg_{Cu}^{-1} h^{-1} and 100% selectivity at 250 °C and under a pressure of 40 bar with a H_2/CO_2 ratio of 3 (Fig. 5; Table 2, entry 2).

Due to the photothermal effect, the plasmonic Ag and Au NPs can increase the reaction temperature after the irradiation of light. Zeng and co-workers prepared Au&Pt@ZIF-8 *via* the encapsulation of Pt nanocubes and Au nanocages into ZIF-8, in which the Au nanocages transformed light to thermal energy, the Pt nanocubes served as the catalyst toward CO_2 hydrogenation, ZIF-8 functioned as "heat insulators" to prevent heat from dispersing in solution [38]. Au&Pt@ZIF displayed a high TOF value of 1522 h^{-1} for the synthesis of methanol under the light irradiation, which was 13 times higher than the controlled experiment in the dark (Table 2, entry 3). The high catalytic performance can be maintained for 6 runs.

3.3.2. CO_2-to-$HCOO^-$

Byers and Tsung *et al.* developed an active catalyst of Ru@UiO-66 for the hydrogenation of CO_2 to formate (Fig. 6) [39]. (^{tBu}PNP)

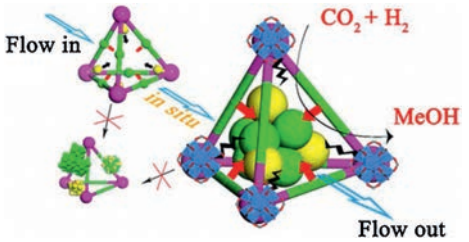

Fig. 5. Catalytic behavior of Cu/ZnOx@UiO-bpy composite in CO_2 hydrogenation. Reproduced with permission [37]. Copyright 2017, American Chemical Society.

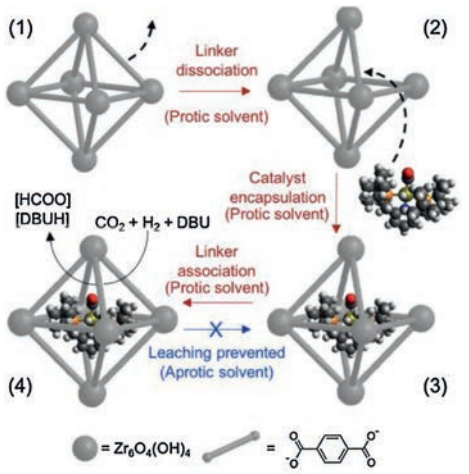

Fig. 6. Catalysis in MOFs using aperture-opening encapsulation. Reproduced with permission [39]. Copyright 2018, American Chemical Society.

Ru(CO)HCl (^{tBu}PNP = 2,6-bis((di-*tert*-butyl-phosphino)methyl) pyridine) was used for the precursor. Catalytic CO_2 hydrogenation studies were studied at 27 °C and under 15 bar with a H_2/CO_2 ratio of 4, which showed that Ru@UiO-66 gave rise to $HCOO^-$ with a TOF value of 6×10^5 h^{-1} (Table 2, entry 4). Moreover, Ru@UiO-66 can be recycled for 5 runs without loss of activity.

3.3.3. CO_2-to-CH_4

CO_2 hydrogenation can also produce CH_4, which is also called the Sabatier reaction and is an important catalytic process to eliminate the CO_2 concentration and generate the clean CH_4 fuel. Lu and co-workers prepared Ni@MOF-5, in which Ni NPs were highly dispersed (41.8%) over MOF-5 [40] (Table 2, entry 5). The Ni@MOF-5 composite showed high activity at low temperature and exhibited almost no deactivation in the long-term stability tests up to 100 h.

Later, this group reported a 20Ni@MIL-101 (where 20 indicate that the nickel loading was 20%) composite by encapsulating Ni NPs in MIL-101 *via* a double solvent method (DSM) [41]. 20Ni@MIL-101 exhibited a high thermal stability and a low

activation energy (88 kJ/mol) for CO_2 hydrogenation, giving rise to CH_4 with a high TOF value of 1.63×10^{-3} s^{-1} at 300 °C (Table 2, entry 6). The density-functional theory (DFT) calculations uncovered that the potential energy barrier was about 10.0 kcal/mol for CO_2 dissociation into CO_{ads} and O_{ads} over the Ni (1 1 1) surface, which was lower than Ni (200) plane (20.3 kcal/mol).

Cheang and Xu *et al*. prepared a Ni@UiO-66 composite through the adsorption of Ni^{2+} ions into the cavity of UiO-66, and then *in situ* reduction under a 5% H_2/Ar atmosphere at 250 °C (Fig. 7) [42]. The uniform distribution of Ni NPs with an average size of 2 nm throughout the UiO-66 framework was revealed by the HAADF-STEM and EDX elemental mapping. Compared with Ni/ZrO_2 and Ni/SiO_2, Ni@UiO-66 exhibit outstanding activity and high selectivity for CO_2 methanation at low temperatures (Table 2, entry 7), which is due to the good dispersion of ultrasmall Ni NPs and the low activation energy (E_a = 68.9 kJ/mol).

3.4. CO_2 photoreduction

3.4.1. MNPs@MOFs or MNPs/MOFs

CO_2 photoreduction is a process that uses renewable solar energy to transform CO_2 into products with different oxidation state, *e.g.*, $HCOO^-$, CO, CH_3OH and CH_4. MOFs have been extensively studied for heterogeneous CO_2 reduction, but however, the catalytic efficiency is far from satisfactory. The efficiency can be improved through incorporating precious metal nanoparticles to MOFs to form MNPs@MOFs (or MNPs/MOFs. MNPs@MOFs herein refers to that the MNPs are incorporated into the inner cavities of the MOFs, while MNPs/MOFs refers to that the MNPs are loaded on the external surfaces of the MOFs): 1) MNPs can serve as electrons trapping sites, promote the charge separation, suppress the electron-hole recombination, and behave as active reaction sites for the CO_2 reduction [43,44]; 2) Some noble MNPs such as Cu, Ag and Au NPs display localized surface plasmon resonance (LSPR) effect, which can boost the visible-light harvesting capabilities of MOFs composites [45–48].

The doping of noble metals such as Pt and Au into the MOFs is generally a feasible strategy to inhibit the recombination of the photo-generated electrons and holes [43,44]. Wang and Sun *et al*. embedded Pt NPs inside and/or outside of NH_2-UiO-68 [43]. As for 2 wt% Pt@NH_2-UiO-68, in which Pt NPs were located inside NH_2-UiO-68, showed the highest CO_2 photoreduction activity (66.7 μmol g^{-1} h^{-1} for CO) under visible light irradiation (Table 3, entry 1). Pt NPs with an appropriate location and content in the resulting composites could facilitate the contact between Pt NPs and NH_2-UiO-68, thereby achieving efficient charge transfer in the photocatalytic process. More importantly, an effective charge transfer from NH_2-UiO-68 to the excited Pt NPs *via* the Schottky junction could inhibit the recombination of photogenerated charge carriers.

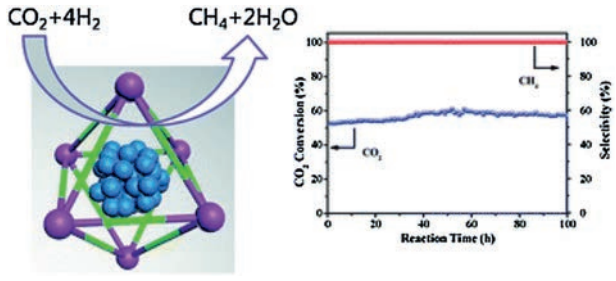

Fig. 7. Ni@UiO-66 composite give both excellent activity and selectivity for CO_2 methanation at low temperature. Reproduced with permission [42]. Copyright 2018, Royal Society of Chemistry.

Zhang and Li *et al*. prepared M-doped NH_2-MIL-125(Ti) (M = Pt and Au) composites and studied their catalytic applications in CO_2 photoreduction under visible-light irradiations in the presence of TEOA [44]. Pt and Au NPs played different effects on the catalytic performances. Compared to NH_2-MIL-125(Ti), Pt/NH_2-MIL-125(Ti) showed an enhanced activity for formate production, whereas Au/NH_2-MIL-125(Ti) had a negative effect on this reaction (Table 3, entries 2 and 3). Based on ESR and DFT calculations, the mechanism studies about Pt/NH_2-MIL-125(Ti)-catalyzed reaction disclosed that the hydrogen could spillover from Pt to the bridging oxygen atoms that were linked to Ti atoms, resulting in the formation of Ti^{3+} and an improved performance for CO_2 reduction to generate formate. However, it is unlikely to happen for Au/NH_2-MIL-125(Ti), which might explain its lower reaction efficiency.

Yang and Yaghi *et al*. reported a core-shell Ag⊂Re_3MOF composite, which was prepared by coating the Re_3-MOF layers onto the pre-synthesized Ag nanocubes (98 nm) (Fig. 8) [45]. The strong quadrupolar LSPR scattering peak ($\lambda_{max} \sim 480$ nm) of Ag nanocube overlaped with the absorption range of the Re_3MOF (400 nm $< \lambda <$ 550 nm). And therefore, Ag⊂Re_3MOF could maintain the characteristic LSPR features of the Ag nanocubes, and meanwhile the photoactive Re centers were spatially confined to the intensified near-surface electric fields at the surface of Ag nanocubes, contributing to a 7-fold enhancement of CO_2-to-CO conversion under visible light compared to Re_3MOF (Table 3, entry 4).

Owing to the LSPR characteristic of Ag NPs, the decorating Ag NPs onto the MOFs surface can further expand the absorption capability of the resultant Ag/MOF composites to the near IR region [46–48]. Huang, Sun and coworkers prepared Ag/MIL-101(Cr) in which Ag NPs with the size range of 80−800 nm were well-dispersed on the outer surface of the MIL-101(Cr) framework [46]. Catalytic studies showed that the photocatalytic activity of Ag/MIL-101(Cr) exhibited a strong dependence on the composite size of MIL-101(Cr), and the highest CO_2 photocatalytic reduction activities up to 808.2 and 427.5 μmol g^{-1} h^{-1} for CO and CH_4, respectively (Table 3, entry 5), were achieved when the size of Ag/MIL-101(Cr) was reduced to 80 nm. A set of photochemical and electrochemical studies revealed that the high catalytic performance might be ascribed to the high density of unit cells on corners and edges of Ag/MIL-101(Cr), which was beneficial to the electron transfer in the photocatalytic CO_2 reduction.

Chen, Duan and co-workers have loaded the plasmonic Au NPs on the surface of a thin porphyrin paddle-wheel framework-3 (PPF-3) nanosheets by electrostatic interaction, giving rise to the Au/PPF-3 composites [47]. The Au NPs could serve as the light-harvesting antenna due to its strong SPR absorption peaks at 525 nm. The Au/PPF-3 composite showed a high photocatalytic activity for CO_2 reduction into $HCOO^-$ with an average production rate of 42.7 μmol g^{-1} h^{-1} under visible-light irradiation (Table 3, entry 6), which was around 4-fold higher than that of the pristine PPF-3. Further mechanism studies disclosed that the catalytic efficiency improvement of CO_2 conversion into $HCOO^-$ over Au/PPF-3was through a plasmon resonance energy transfer process from AuNPs to PPF-3 (Fig. 9).

The product selectivity of CO_2 reduction in the presence of MNPs@MOFs can be summarized as follow: Au/MOFs generate $HCOO^-$, Pt@MOFs or Pt/MOFs give rise to the production of CO or $HCOO^-$, whereas Ag/MOFs composites produce CO or CH_4.

3.4.2. Molecular catalysts@MOFs

The incorporation of molecular catalysts or photosensitizers into the pores of MOFs provides an efficient way to engineer the MOF composites for enhanced photocatalytic CO_2 reduction [49,50]. Fontecave, Mellot-Draznieks and co-workers immobilized the molecular catalyst $[Cp^*Rh(4,4'\text{-bpydc})]^{2+}$ and the

Table 3
Application of MOF composites in the photocatalytic CO_2 reduction.

Entry	MOF composite	Light source	Proton donor	Main carbon product	Photocatalytic reactivity	Ref.
1	Pt@NH_2-UiO-68	400 nm ≤ λ ≤ 780 nm	TEOA	CO	66.7 μmol g^{-1} h^{-1}	[43]
2	Au/NH_2-MIL-125(Ti)	420 nm ≤ λ ≤ 800 nm	TEOA	$HCOO^-$	22.7 μmol g^{-1} h^{-1}	[44]
3	Pt/NH_2-MIL-125(Ti)	420 nm ≤ λ ≤ 800 nm	TEOA	$HCOO^-$	32.4 μmol g^{-1} h^{-1}	[44]
4	Ag ⊂ Re_3MOF	420 nm ≤ λ ≤ 800 nm	TEA	CO	~2.8 (TON)	[45]
5	Ag/MIL-101(Cr)	420 nm ≤ λ ≤ 800 nm	TEOA	CO, CH_4	808.2 μmol g^{-1} h^{-1} (CO) 427.5 μmol g^{-1} h^{-1} (CH_4)	[46]
6	Au/PPF-3	Visible-light	EtOH	HCOOH	42.7 μmol g^{-1} h^{-1}	[47]
7	Rh–Ru@MIL-101-NH_2	λ > 415 nm	TEOA	$HCOO^-$	13.2 μmol g^{-1} h^{-1}	[49]
8	Ni@Ru-UiO-67	λ = 450 nm	TEOA	CO	581 (TON)	[50]
9	$CsPbBr_3$@ZIF-67	100 W Xe lamp	H_2O	CO, CH_4	0.77 μmol g^{-1} h^{-1} (CO) 3.51 μmol g^{-1} h^{-1} (CH_4)	[51]
10	$CsPbBr_3$@ZIF-8	100 W Xe lamp	H_2O	CO, CH_4	0.51 μmol g^{-1} h^{-1} (CO) 1.81 μmol g^{-1} h^{-1} (CH_4)	[51]
11	$MAPbI_3$@PCN-221(Fe)	300W Xe-lamp	H_2O	CO, CH_4	6.6 μmol g^{-1} h^{-1} (CO) 12.9 μmol g^{-1} h^{-1} (CH_4)	[52]
12	Zn_2GeO_4/ZIF-8	500 W xenon arc lamp	H_2O	CH_3OH	0.22 μmol g^{-1} h^{-1}	[56]
13	Zn_2GeO_4/Mg-MOF-74	200 nm ≤ λ ≤ 1100 nm	H_2O	CO	71.9 μmol g^{-1} h^{-1} (CO)	[57]
14	CdS/UiO-bpy/$CoCl_2$	λ ≥ 420 nm	TEOA	CO	235 μmol g^{-1} h^{-1} (CO)	[60]
15	CPO-27-Mg/TiO_2	4 W UV lamps	H_2O vapor	CO, CH_4	409 μmol g^{-1} h^{-1} (CO) 235 μmol g^{-1} h^{-1} (CH_4)	[62]
16	Co-ZIF-9/TiO_2	200 nm ≤ λ ≤ 900 nm	H_2O	CO, CH_4	17.6 μmol g^{-1} h^{-1} (CO) 2.0 μmol g^{-1} h^{-1} (CH_4)	[63]
17	UiO-66/CNNS	400 nm < λ < 800 nm	TEOA	CO	9.9 μmol g_{CN}^{-1} h^{-1}	[69]
18	(Zr-PMOF)/ultrathin g-C_3N_4	λ > 420 nm	H_2O	CO	5.5 μmol g^{-1} h^{-1}	[70]
19	UiO-66-NH_2/2.0graphene	λ > 410 nm	TEOA	$HCOO^-$, CH_4	418.8 μmol g^{-1} h^{-1} ($HCOO^-$) 11.3 μmol g^{-1} h^{-1} (CH_4)	[71]
20	Al-PMOF/NH_2-rGO (5 wt%)	Visible-light	TEOA	$HCOO^-$	685.6 μmol g^{-1} h^{-1}	[72]

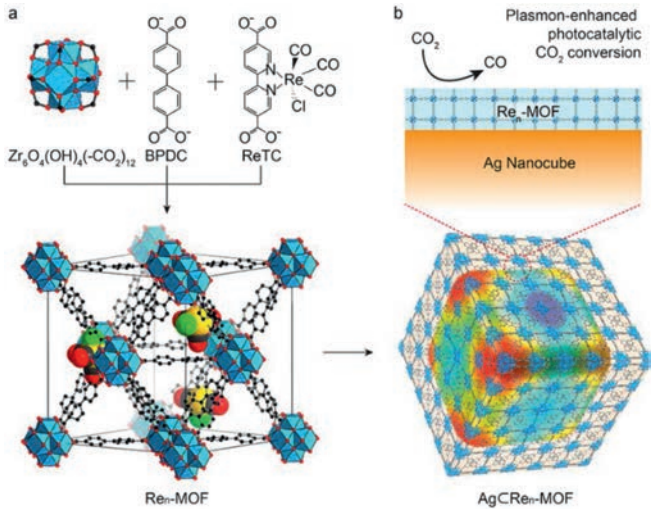

Fig. 8. Structures of Re_n-MOF and Ag⊂Re_n-MOF for plasmon-enhanced photocatalytic CO_2 conversion. Reproduced with permission [45]. Copyright 2017, American Chemical Society.

photosensitizer $[Rh(bpy)_2(4,4'\text{-bpydc})]^{2+}$ into the highly porous MIL-101-NH_2(Al) *via* an easy post-synthetic impregnation, giving rise to the Rh–Ru@MIL-101-NH_2 composites [49]. The large cavity of MIL-101-NH_2(Al) as a nanoreactor allowed the intimate confinement of the catalyst and the photosensitizer. Catalytic studies showed that Rh–Ru@MIL-101-NH_2 exhibited a remarkable selectivity towards CO_2 reduction under visible light irradiation, and produced $HCOO^-$ with the rate of 13.2 μmol g^{-1} h^{-1} (Table 3, entry 7). The H_2 production was totally suppressed, which was in deep contrast to the molecular catalyst alone. There was a negligible leaching of the active species in Rh–Ru@MIL-101-NH_2 during photocatalysis, which was due to the strong host–guest interactions.

Using the "ship-in-bottle" synthetic strategy, Jin and Kong *et al.* encapsulated a molecular catalyst $[Ni^{II}(bpet)(H_2O)_2]$ (bpet = 1,2-bis((pyridin-2-ylmethyl)thio)ethane) into a highly robust and visible-light responsive Ru-UiO-67 to obtain Ni@Ru-UiO-67 (Fig. 10) [50]. Ni@Ru-UiO-67 exhibited an efficient CO_2 reduction to CO with a TON of 581 and a high selectivity of 99% under the irradiation with a LED light (82 W) (Table 3, entry 8). Photoluminescence (PL)

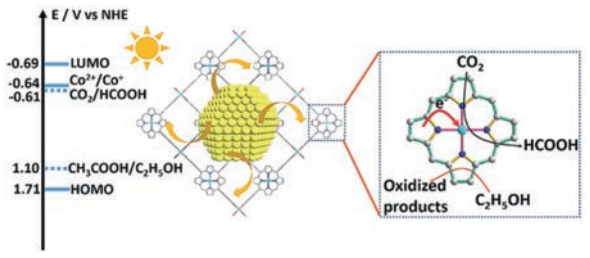

Fig. 9. Proposed mechanism for plasmon-enhanced photocatalytic activity of Au/PPF-3 towards CO_2 reduction. Reproduced with permission [47]. Copyright 2019, Royal Society of Chemistry.

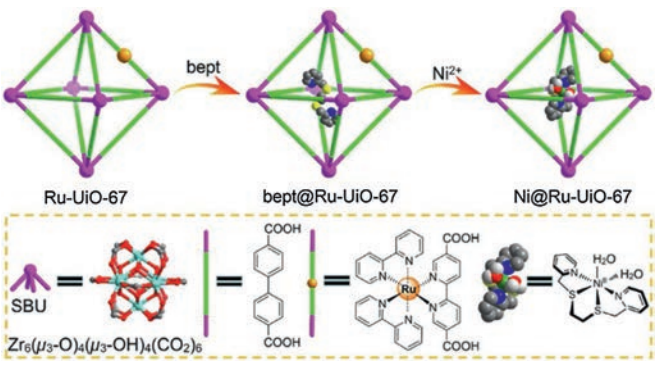

Fig. 10. Schematic illustration for "Ship-in-a-Bottle" synthetic strategy to prepare Ni@Ru-UiO-67 composite. Reproduced with permission [50]. Copyright 2019, Elsevier.

measurements showed the facile electron transfer from the excited Ru-MOFs to the encapsulated Ni(II) complex, which was crucial for the excellent activity of Ni@Ru-UiO-67. Advanced ultrafast absorption spectroscopy and DFT calculations further disclosed that the photoelectrons that were produced by the Ru ligand could transfer to the Ni(II) complex, affording Ni^0 species for the reduction CO_2 to CO.

3.4.3. QDs@MOFs

QDs are fluorescent semiconductor nanoparticles with the size range of 1–10 nm, which possess high quantum yield and strong light capture ability. Engineering MOFs and QDs to form QDs@MOFs can accelerate the separation of photogenerated charges, inhibit the recombination of photogenerated electrons and holes, and thus enhance the photocatalytic performance of the resultant composites due to the close inter-face and matched band gap between QDs and MOFs [51,52].

Chen's group immobilized ZIF-8 and ZIF-67 on the surface of $CsPbBr_3$ quantum dot to afford $CsPbBr_3$@ZIFs with an improved moisture stability, photo-generated charge separation efficiency and CO_2 capturing ability [51]. $CsPbBr_3$@ZIF-67 exhibited the broadened visible light absorption that was extended to 620 nm. The inhibited photo-generated carrier radiative recombination and effective electron transfer between $CsPbBr_3$ and ZIFs were confirmed by the steady-state and time-resolved photoluminescence studies. The Co^{II} center in ZIF-67 served as an electron reservoir to accelerate the separation of photo-induced carriers. Catalytic studies showed that only CO and CH_4 were detected, and the yield of CH_4 (10.5 μmol/g) was much higher than that of CO (2.3 μmol/g). The higher selectivity of CH_4 was attributed to the solid-gas mode catalytic reaction condition with water vapor involved, which can provide sufficient protons and help to overcome the dynamic barrier to produce CH_4. Moreover, Both $CsPbBr_3$@ZIF-8 and $CsPbBr_3$@ZIF-67 exhibited enhanced CO_2 reduction activities, which were 1.39- and 2.66-fold, respectively, of the naked $CsPbBr_3$ (Table 3, entries 9 and 10).

Zhang and Lu *et al*. prepared a series of $MAPbI_3$@PCN-221(Fe_x) (x = 0–1) composites by encapsulating $CH_3NH_3PbI_3$ ($MAPbI_3$) perovskite QDs in the pores of PCN-221(Fe) through a sequential deposition route (Fig. 11) [52]. As revealed by the steady-state and time-resolved photoluminescence experiments, the photo-generated electrons of the encapsulated $MAPbI_3$ QDs under light irradiation quickly transferred to the photocatalytic Fe-porphyrin units of PCN-221(Fe), and thereby an efficient charge separation between the perovskite QDs and the MOF was achieved. Catalytic results disclosed that a high total yield of 1559 μmol/g for photocatalytic CO_2 reduction to CO (34%) and CH_4 (66%) was achieved using water as an electron source, which was 38 times higher than that of PCN-221($Fe_{0.2}$) in the absence of perovskite QDs (Table 3, entry 11).

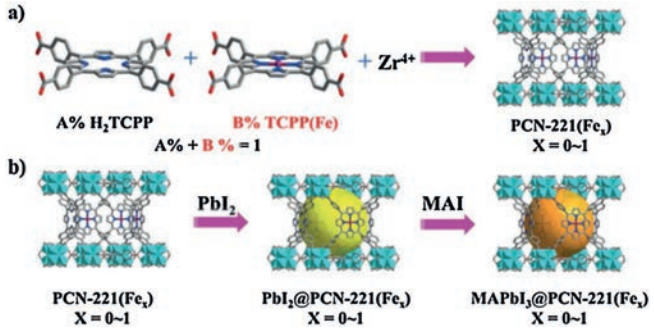

Fig. 11. Schematic illustrations for the synthesis of a) PCN-221(Fe_x), and b) $MAPbI_3$ QDs (large spheres) encapsulated in the pores of PCN-221(Fe_x) by a sequential deposition route. Reproduced with permission [52]. Copyright 2019, Wiley-VCH.

3.4.4. MOFs/semiconductors

Coupling MOFs with semiconductors has been proved to be an effective strategy to boost the catalytic performance in the photocatalytic CO_2 reduction. The resultant MOF composites can display an improved separation efficiency of photo-generated electrons. The most common semiconductors that are used in the MOFs composites fabrication include Zn_2GeO_4, CdS, TiO_2 and carbon nitride.

Zn_2GeO_4 is widely used in the photocatalytic reduction of CO_2, which shows high crystallinity and light/thermal stability, but the weak CO_2 adsorption and low solar energy utilization efficiency largely inhibit its practical applications [53–55]. To overcome these shortcomings, Wang *et al*. immobilized ZIF-8 nanoparticles on the surfaces of Zn_2GeO_4 nanorods to obtain the ZIF-8/Zn_2GeO_4 composite, which inherited the high CO_2 adsorption property of ZIF-8 and the high crystallinity of Zn_2GeO_4 (Fig. 12) [56]. ZIF-8/Zn_2GeO_4 with 25 wt% ZIF-8 displayed 3.8 times higher CO_2 uptake than Zn_2GeO_4, which could effectively absorb CO_2 that was dissolved in water. Catalytic studies showed that ZIF-8/Zn_2GeO_4 exhibited 62% enhancement in photocatalytic conversion of CO_2 into CH_3OH (Table 3, entry 12).

Later, Gao and Cao *et al*. prepared Mg-MOF-74/Zn_2GeO_4 through a hydrothermal method, and a close interaction was formed between Zn_2GeO_4 and Mg-MOF-74 [57]. The composite displayed high efficiency in photocatalytic CO_2 to CO using only water as the sacrificial agent, with an evolution rate of 71.9 μmol g^{-1} h^{-1}, which was 7 times higher than that of Zn_2GeO_4 (Table 3, entry 13). The enhanced photocatalytic performances were attributed to the higher CO_2 adsorption and the slower recombination of photo-generated e-h pairs of Mg-MOF-74/Zn_2GeO_4 than Zn_2GeO_4. Mechanistic studies disclosed that the photo-generated electrons could effectively transfer from Zn_2GeO_4 to the open alkaline metal sites (Mg^{2+}) of Mg-MOF-74 for the subsequent CO_2 reduction.

As an excellent visible-light response semiconductor, CdS has been extensively used as photo-catalyst for CO_2 reduction, but unfortunately, its applications are limited due to the fast recombination of photo-generated electron-hole pairs, the serious photo-corrosion, and the low CO_2 adsorption capability [58,59]. Wu, Han and co-workers fabricated a ternary CdS/UiO-bpy/$CoCl_2$ composites, in which the semiconductor CdS and the molecular redox catalyst $CoCl_2$ were integrated through UiO-bpy [60]. The composite was highly efficient in the photocatalytic conversion of CO_2 to CO under visible light irradiation, giving rise to an evolution rate of 235 μmol g^{-1} h^{-1} and 85% selectivity (Table 3, entry 14).

TiO_2 is a benchmark inorganic semiconductor for CO_2 photoreduction [61]. Li *et al*. prepared a CPO-27-Mg/TiO_2 composite through an *in situ* growth method, which was composed of TiO_2 nanospheres that grew on the surfaces of spindle-shaped CPO-27-Mg microcrystal [62]. The coordination between the carboxylate groups of CPO-27-Mg and Ti^{4+} of TiO_2 resulted in the intimate contact between MOF and semiconductor (Fig. 13). Catalytic studies showed that CPO-27-Mg/TiO_2 exhibited an

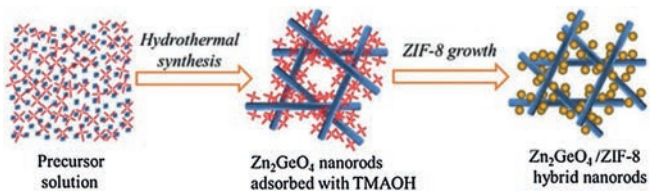

Fig. 12. Synthesis of ZIF-8/Zn_2GeO_4 composite. Reproduced with permission [56]. Copyright 2019, Royal Society of Chemistry.

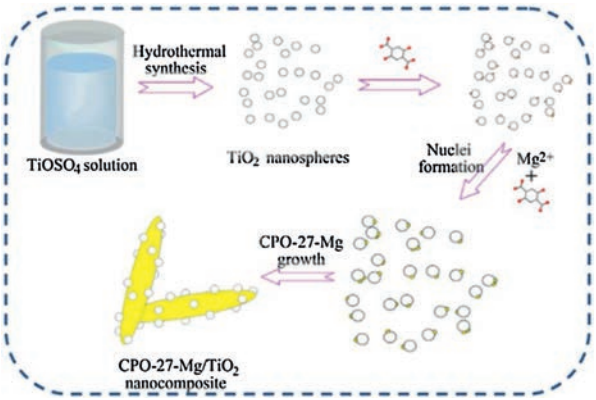

Fig. 13. Schematic illustration of the formation of CPO-27-Mg/TiO_2 nanocomposite. Reproduced with permission [62]. Copyright 2016, Elsevier.

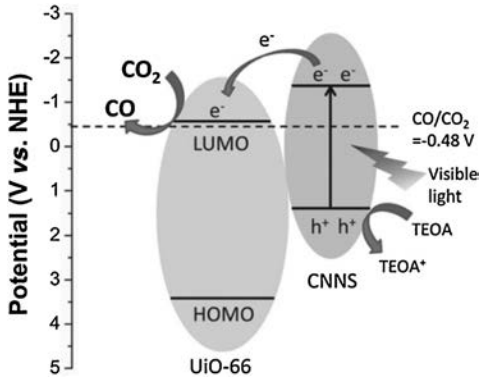

Fig. 14. Proposed mechanism of photocatalytic reduction of CO_2 by the UiO-66/CNNS heterogeneous photocatalyst under visible light irradiation. Reproduced with permission [69]. Copyright 2015, Wiley-VCH.

enhanced performance for the photoreduction of CO_2 to CO and CH_4, and meanwhile the reduction of H_2O to form H_2 was totally inhibited (Table 3, entry 15).

Using a similar strategy, Xu and Ye *et al*. reported a Co-ZIF-9/TiO_2 composite, in which TiO_2 and Co-ZIF-9 were closely bound with each other, thus leading to better charge separation [63]. The composite exhibited an enhanced total utilized photoelectron number (UPN), which was about 2.1 times of the pure TiO_2 (Table 3, entry 16). Linear sweep voltammetry disclosed that a more positive onset potential for CO_2 reduction and higher photocurrent density in the simulated photoelectron reduction of CO_2 was achieved in the composite, which indicated a better CO_2 activation and superior charge separation.

As a metal-free and visible-light active photocatalyst, graphitic carbon nitride (CN) has been applied in the photocatalytic CO_2 reduction [64,65]. However, due to the fast recombination of the photogenerated electron–hole pairs, the efficiency of bulk carbon nitride (bulk CN) is not satisfactory. These drawbacks can be overcome by the exfoliation of bulk CN to 2D atomic carbon nitride nanosheet (CNNS), leading to the improved photocatalytic activity [66–68]. Due to the low CO_2 adsorption capability of carbon nitride, further improvement of the efficiency is still a challenge.

Ye and co-workers prepared a UiO-66/CNNS composite through the electrostatic reaction between the negatively charged nano-sized CNNS and positively charged UiO-66 [69]. As confirmed by the TEM image of the UiO-66/CNNS composite, the CNNS were coated on the surface of UiO-66. Furthermore, the nanojunctions between the UiO-66 crystal and the CNNS were revealed by a distinguished and coherent inter-face HRTEM image, which could give rise to an efficient electron transfer. In addition, the UiO-66/CNNS composite showed a superior CO_2 uptake ability than that of CNNS. Photocatalytic CO_2 reduction in the presence of UiO-66/CNNS produced CO in the yield of 9.9 μmol g_{CN}^{-1} h^{-1}, which was three times than CNNS (Table 3, entry 17). A tentative mechanism for the photocatalytic CO_2 reduction over UiO-66/CNNS was proposed as follow (Fig. 14): upon visible light irradiation, electrons were promoted from the valence band of CNNS to its corresponding conduction band. Then the photogenerated electrons migrated to the surface of CNNS and transferred to UiO-66 across the interface between CNNS and UiO-66. Subsequently, the adsorbed CO_2 was reduced to CO.

Zhang and Zhong *et al*. prepared a series of Zr-porphyrin metal-organic framework (Zr-PMOF)/ultrathin g-C_3N_4 composites, in which hollow Zr-PMOF nanotubes were surrounded by 3D ultrathin g-C_3N_4, leading to an interfacial interaction [70]. The interaction provided a platform for g-C_3N_4 as a conductor to obtain electrons from ligands or as a donor to transfer electrons to Zr-O cluster of Zr-PMOF. The composite exhibited a CO evolution rate of 5.5 μmol g^{-1} h^{-1} in the CO_2 reduction (Table 3, entry 18), which was 2.2 and 3.2 times higher than Zr-PMOFs and g-C_3N_4, respectively.

3.4.5. MOFs/graphene

To improve the conductivity of MOFs, engineering MOFs/graphene composites is a feasible strategy, considering that graphene has unique two-dimensional structure, outstanding electrical and thermal properties, and efficient electron transfer ability. Therefore, MOFs/graphene composites would be promising materials for photocatalytic reactions [71,72].

Li's group prepared UiO-66-NH_2/graphene composite *via* a microwave-induced synthesis route by *in situ* assembly of UiO-66-NH_2 onto graphene [71]. UiO-66-NH_2 crystals were highly dispersed on the surface of graphene, and the tight junctions between UiO-66-NH_2 and the surface of graphene was formed. The UiO-66-NH_2/2.0graphene composite displayed a strong CO_2 uptake about 73 cm^3/g. Catalytic studies showed that UiO-66-NH_2/2.0graphene exhibited a high activity (418.8 μmol g^{-1} h^{-1}) and good selectivity (78.6%) in the photocatalytic CO_2 to formic acid under visible-light irradiation (λ > 410 nm, 300 W Xe lamp) (Table 3, entry 19). Controlled experiments disclosed that the introduction of graphene could suppress the competitive reaction of hydrogen evolution. The high CO_2 photo-reduction activity and excellent recyclability might attribute to the highly dispersion of UiO-66 ultrafine nanocrystals on the surfaces of graphene and the strong interaction between UiO-66 and graphene (Fig. 15).

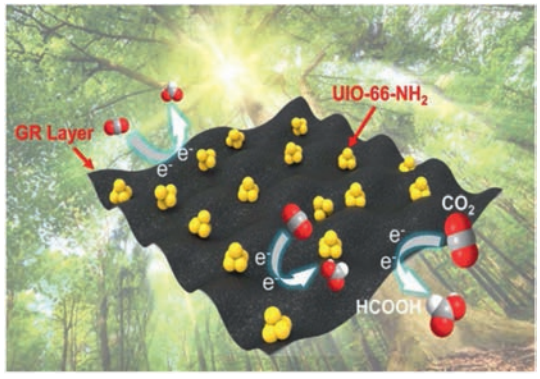

Fig. 15. The working mechanism of the UiO-66-NH_2/2.0graphene composite for reducing CO_2 to formic acid under visible light irradiation. Reproduced with permission [71]. Copyright 2018, Elsevier.

Do and co-workers prepared Al-PMOF/NH_2-rGO (GO = graphene oxide) that was composed of a porphyrin metal–organic framework Al-PMOF and amine-functionalized graphene (NH_2-rGO) [72]. Photoluminescence and Mott-Schottky measurements disclosed that the band gap was decreased and electron–hole recombination was suppressed in the resultant composite. In the presence of Al-PMOF/NH_2-rGO (5 wt%), photoreduction of CO_2 under visible light irradiation in the presence of TEOA as a sacrificial agent led to the formation of $HCOO^-$ with almost 100% selectivity and an evolution rate of 685.6 μmol g^{-1} h^{-1} under visible light irradiation (Table 3, entry 20), which was 76% greater than that of Al-PMOF. The N species on the rGO contributed to the catalytic efficiency of Al-PMOF/NH_2-rGO (5 wt%) in two ways: firstly, the N species on rGO enabled the connection of PMOF with the graphene and electron transfer from the excited PMOF to the graphene sheet; secondly, the amine groups of rGO could also absorb light and thereby boost the light-harvesting capability of the composite. The proposed reaction mechanism was illustrated as following: After being excited under light illumination, the ligand TCPP in Al-PMOF behaved as a visible-light-harvesting unit, and the electrons transferred from TCPP to graphene while the holes remained in the TCPP. Subsequently, the electrons from graphene transferred to the adsorbed CO_2 and led to the reduction of CO_2 towards $HCOO^-$ in the presence of TEOA acting as a hydrogen source.

3.5. CO_2 electroreduction

Electrochemical reduction of CO_2 using renewable energy is one of the most promising approaches for CO_2 conversion to valuable products. The main challenges lie in the field of CO_2 electroreduction are the low selectivity, faradaic efficiency and catalytic efficiency.

Li and Bao *et al*. reported electrocatalytic applications of Ag_2O/ZIF-7, which was prepared through one-pot hydrothermal treatment of ZIF-7 in $AgNO_3$ aqueous solution [73]. Catalytic studies disclosed that the faradaic efficiency and current density of Ag_2O/layered ZIF composite for CO_2 electroreduction to CO reached 80.5% and 26.2 mA/cm^2 at -1.2 V *vs*. the reversible hydrogen electrode (RHE), respectively, under CO_2-saturated 0.25 mol/L K_2SO_4 solution (Table 4, entry 1).

Yu and Qiu *et al*. fabricated Cu_2O@Cu-MOF for the electrochemical reduction of CO_2 [74]. Catalytic studies disclosed that the Cu_2O@Cu-MOF exhibited an excellent performance with a 79.4% faradaic efficiency for hydrocarbon (CH_4+C_2H_4), and especially 63.2% faradaic efficiency for CH_4 (Table 4, entry 2). The high electrocatalytic activity and high selectivity to CH_4 was attributed to the multiple functionalities of Cu_2O@Cu-MOF, such as absorption, activation, and catalysis derived from synergistic effects of Cu-MOF and Cu_2O.

Metallocene complexes (MCp_2, Cp stands for cyclopentadienyl) are electron-rich with high stability and aromaticity, which can serve as potential electron donator and carrier to enrich the electron density of MOFs [75]. Chen and Lan *et al*. developed a $CoCp_2$@MOF-545-Co composite for the highly selective CO_2 electroreduction [76]. The composite was prepared by the incorporation of $CoCp_2$ into the pores of MOF-545, which display high porosity, large pore size (3.6 nm) and excellent chemical/thermal stability that can serve as an ideal platform to interact with $CoCp_2$. In the resultant $CoCp_2$@MOF-545-Co composite, the π-electron system of cyclopentadienyl ring might overlap with π-electron system of porphyrin, which would endow MOF-545 with higher CO_2 adsorption capability, larger number of active sites and more favorable electron transfer property to largely enhance the electrocatalytic activity. Catalytic studies disclosed that $CoCp_2$@-MOF-545-Co selectively converted CO_2 to CO with 97% Faradaic efficiency under CO_2-saturated 0.5 mol/L $KHCO_3$ (pH 7.2) solution (Table 4, entry 3). Mechanistic studies suggested that the continuous electron transfer channel in MOFs could be created through the introduction of metallocene, and meanwhile the adsorption energy of CO_2 can be largely reduced by the strong binding-interaction with metalloporphyrin, which contributed to the excellent activity of $CoCp_2$@MOF-545-Co in the CO_2 electroreduction (Fig. 16).

3.6. CO_2 photoelectroreduction

An alternative approach for CO_2 transformation is the CO_2 photoelectroreduction, which integrates photocatalysis and electrocatalysis [11]. Photoelectrocatalytic reduction of CO_2 would reduce electricity consumption as compared to the CO_2 electroreduction because of the introduction of solar energy. Moreover, as compared to CO_2 electroreduction, CO_2 photoelectroreduction may achieve higher efficiency because the applied external bias voltage can drive the separation of photo-generated electrons and holes, which is the most crucial step in limiting the photocatalytic efficiency.

Cardoso and co-workers reported the synthesis of Ti/TiO_2NT-ZIF-8 composite for the photoelectrocatalytic reduction of CO_2 to produce CH_3OH and C_2H_5OH (Fig. 17) [77]. The composite was

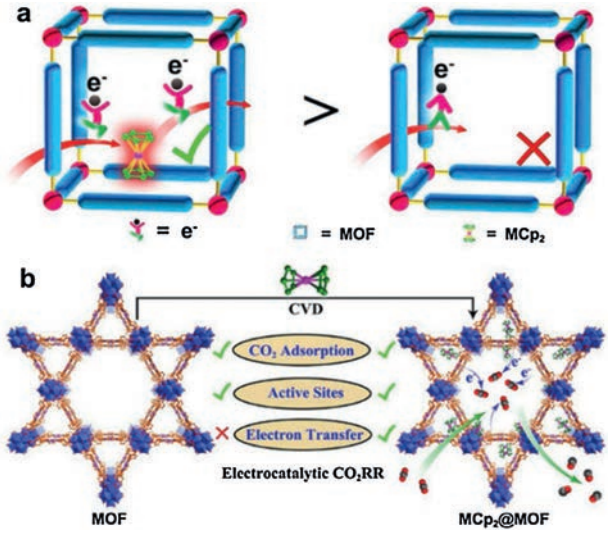

Fig. 16. The schematic presentation for the advantages of MCp_2@MOF in electrocatalytic CO_2RR. Reproduced with permission [76]. Copyright 2020, Elsevier.

Table 4
Application of MOF composites in the electrocatalytic CO_2 reduction.

Entry	Electrode	Electrolyte	Potential	Main carbon product	Faradaic efficiency (%)	Ref.
1	Ag_2O/layered ZIF	0.25 mol/L K_2SO_4	− 1.2 V *vs*. RHE	CO	80.5	[73]
2	Cu_2O@Cu-MOF	0.1 mol/L $KHCO_3$	− 1.71 V *vs*. RHE	CH_4, C_2H_4	63.2 (CH_4); 16.2 (C_2H_4)	[74]
3	$CoCp_2$@MOF-545-Co	0.5 mol/L $KHCO_3$	− 0.7 V *vs*. RHE	CO	97	[76]

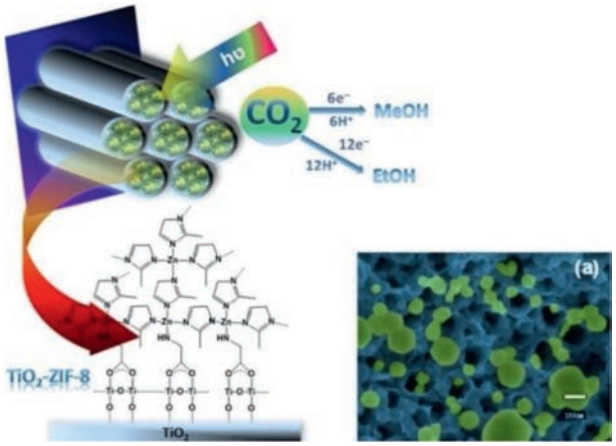

Fig. 17. The schematic presentation of Ti/TiO_2NT-ZIF-8 composite for the photoelectrocatalytic reduction of CO_2 to produce methanol and ethanol fuels. Reproduced with permission [77]. Copyright 2018, Elsevier.

prepared by the growth of ZIF-8 nanoparticles on the Ti/TiO_2 nanotubes through a layer-by-layer process. Photoelectrocatalysis of the Ti/TiO_2NT-ZIF-8 electrodes gave rise to the formation of up to 0.7 mmol/L of CH_3OH and 10 mmol/L of ethanol in 0.1 mol/L Na_2SO_4 at room temperature. The ZIF-8 not only participated in the CO_2 adsorption/activation, but also functionalized as a co-catalyst.

4. Conclusion and future outlook

In summary, the syntheses and catalytic applications of MOF composites towards CO_2 capture and conversion (C3), including chemical fixation, hydrogenation, photoreduction, electroreduction and photoelectroreduction of CO_2 have been discussed. Although MOF composites have great potentials towards C3 application, this research field is still in its infancy: Firstly, the chemical and thermal stability of MOF composites should be further improved. Secondly, the scalable and efficient preparation methods for MOF composites are highly desired. Until now, the fabrication of MOF composites for the target CO_2 conversion is still in the laboratory scale by time-consuming procedures, which restricts their industrial-scale applications. Thirdly, a deep understanding of the interactions between MOFs and functional materials is still not sufficient. In-depth studies of the interfacial interactions can guide the design of the next generation of MOF composites for CO_2 activation.

For the CO_2 chemical fixation, more types of transformations should be explored to convert CO_2 into abundant value-added chemicals, which will open new ways for the CO_2 utilization using MOF composites as catalysts. And especially, MOF composites that can promote the transformations of CO_2 at room temperature, atmospheric pressure and low CO_2 concentrations are highly desired, but however only a few relevant studies have been reported. As for the CO_2 hydrogenation, MOF composites that can promote the reaction under atmospheric pressure and room temperature are highly desired, considering that some MOFs are unstable at high temperatures.

For the photocatalytic reduction of CO_2, several problems remain to be solved. Firstly, the main products of MOF composites for the photocatalytic CO_2 reduction are limited to C_1 compounds (*e.g.* CO, CH_4, HCOOH and CH_3OH) and C_2 compound (*e.g.* CH_3CH_2OH), but the reports about the C_{3+} products (hydrocarbons with more than three carbons) are rare. Secondly, the detailed mechanism of photocatalytic CO_2 reduction on the MOF composites is still unclear. The combination of advanced characterizations and density functional theory calculations should be an efficient way to for the deep study of the structure–activity relationship, which is of vital importance to the rational design of MOF composites. Finally, most of the present catalytic systems need additional sacrificial regents, which is not economically feasible. Coupling the photocatalytic CO_2 reduction with oxidative organic reaction is an efficient strategy to tackle this problem, which produces solar fuel and value-added organic chemicals simultaneously. As for the CO_2 electroreduction, MOF composites that are based on earth-abundant metal elements and possess a good compromise of high faradaic efficiency and selectivity are highly required.

In conclusion, MOF composites as heterogeneous catalysts for the CO_2 capture and conversion are showing bright future and will no doubt attract more attention in the CO_2 chemistry. The next challenge is to tackle the drawbacks of MOFs composites and put them into practical applications.

Declaration of competing interest

The authors declared that they have no conflicts of interest to this work. They also declared that they do not have any commercial or associative interest that represents a conflict of interest in connection with the work submitted.

Acknowledgments

The authors acknowledge the support from the National Natural Science Foundation of China (Nos. 21773314, 21720102007, 21821003 and 21890382), the Guangdong Natural Science Funds for Distinguished Young Scholar (No. 2019B151502017), the Tip-top Youth Talents of Guangdong special support program (No. 20173100042150021), Science and Technology Planning Project of Guangzhou (No. 201707010168), the General Financial Grant from the China Postdoctoral Science Foundation (No. 2019M662809), and Local Innovative and Research Teams Project of Guangdong Peal River Talents Program (No. 2017BT01C161).

References

[1] L. Zhang, J. Liu, C.Y. Su, Application of metal-organic frameworks in CO2 capture and conversion, in: K.T. Mahmudov, M.N. Kopylovich, M.F.C.G. Silva, A. J.L. Pombeiro (Eds.), Noncovalent Interactions in Catalysis, The Royal Society of Chemistry, 2019, pp. 455–478.
[2] Z. Chen, J. Liu, H. Cui, L. Zhang, C.Y. Su, Acta Chim. Sinica 77 (2019) 242–252.
[3] M. Ding, R.W. Flaig, H.L. Jiang, O.M. Yaghi, Chem. Soc. Rev. 48 (2019) 2783–2828.
[4] C.A. Trickett, A. Helal, B.A. Al-Maythalony, et al., Nat. Rev. Mater. 2 (2017) 17045.
[5] J.W. Maina, C. Pozo-Gonzalo, L. Kong, et al., Mater. Horiz. 4 (2017) 345–361.
[6] (a) H. He, J.A. Perman, G. Zhu, S. Ma, Small 12 (2016) 6309–6324;
(b) B. Yu, B. Zou, C.W. Hu, J. CO2 Util. 26 (2018) 314–322;
(c) K.H. Chen, H.R. Li, L.N. He, Chin. J. Org. Chem. (2020), doi:http://dx.doi.org/10.6023/cjoc202004030.
[7] Y. Shi, S. Hou, X. Qiu, B. Zhao, Topics Curr. Chem. 378 (2020) 11.
[8] A. Álvarez, A. Bansode, A. Urakawa, et al., Chem. Rev. 117 (2017) 9804–9838.
[9] D. Li, M. Kassymova, X. Cai, S.Q. Zang, H.L. Jiang, Coord. Chem. Rev. 412 (2020) 213262.
[10] R. Wang, F. Kapteijn, J. Gascon, Chem. Asian J. 14 (2019) 3452–3461.
[11] S. Xie, Q. Zhang, G. Liu, Y. Wang, Chem. Commun. 52 (2016) 35–59.
[12] S.L. Hou, J. Dong, B. Zhao, Adv. Mater. (2019) 1806163.
[13] J. Liu, L. Chen, H. Cui, et al., Chem. Soc. Rev. 43 (2014) 6011–6061.
[14] X. Liang, L. Chen, L. Zhang, C.Y. Su, Chin. Sci. Bull. 63 (2018) 248–265.
[15] L. Zhang, J. Liu, C.Y. Su, Porphyrin metal–organic frameworks in heterogeneous supramolecular catalysis, in: L. Wang, C.Y. Su (Eds.), Supramolecular Catalysts: Design, Fabrication, and Applications, World Scientific Publishing Co. Pte Ltd., 2020, pp. 225–265.
[16] A. Bavykina, N. Kolobov, I.S. Khan, et al., Chem. Rev. 120 (2020) 8468–8535.
[17] G. Li, S. Zhao, Y. Zhang, Z. Tang, Adv. Mater. (2018) 1800702.
[18] Q. Yang, Q. Xu, H.L. Jiang, Chem. Soc. Rev. 46 (2017) 4774–4808.
[19] L. Chen, Q. Xu, Matter 1 (2019) 57–89.
[20] (a) B. Li, J.G. Ma, P. Cheng, Small (2019) 1804849;
(b) L. Chen, X. Zhang, X. Cheng, et al., Nanosc. Adv. 2 (2020) 2628–2647;

(c) T. Wu, X. Liu, Y. Liu, et al., Coord. Chem. Rev. 403 (2020) 213097;
(d) Q.L. Zhu, Q. Xu, Chem. Soc. Rev. 43 (2014) 5468–5512.
[21] M. Ding, H.L. Jiang, ACS Catal. 8 (2018) 3194–3201.
[22] B. Aguila, Q. Sun, X. Wang, et al., Angew. Chem. Int. Ed. 57 (2018) 10107–10111.
[23] G.G. Chang, X.C. Ma, Y.X. Zhang, et al., Adv. Mater. (2019) 1904969.
[24] D. Chen, R. Luo, M. Li, et al., Chem. Commun. 53 (2017) 10930–10933.
[25] C. Liu, X.H. Liu, B. Li, et al., J. Energy Chem. 26 (2017) 821–824.
[26] L.J. Gooßen, N. Rodríguez, F. Manjolinho, P.P. Lange, Adv. Synth. Catal. 352 (2010) 2913–2917.
[27] F. Manjolinho, M. Arndt, K. Gooßen, L.J. Gooßen, ACS Catal. 2 (2012) 2014–2021.
[28] X.H. Liu, J.G. Ma, Z. Niu, G.M. Yang, P. Cheng, Angew. Chem. Int. Ed. 54 (2015) 988–991.
[29] L. Sun, Y. Yun, H. Sheng, et al., J. Mater. Chem. A 6 (2018) 15371–15376.
[30] J. Shi, L. Zhang, N. Sun, et al., ACS Appl. Mater. Interfaces 11 (2019) 28858–28867.
[31] R.A. Molla, K. Ghosh, B. Banerjee, et al., J. Colloid Interf. Sci. 477 (2016) 220–229.
[32] M. Trivedi, Bhaskaran, A. Kumar, et al., New J. Chem. 40 (2016) 3109–3118.
[33] N.N. Zhu, X.H. Liu, T. Li, et al., Inorg. Chem. 56 (2017) 3414–3420.
[34] G. Dutta, A.K. Jana, D.K. Singh, M. Eswaramoorthy, S. Natarajan, Chem. Asian J. 13 (2018) 2677–2684.
[35] M. Behrens, F. Studt, I. Kasatkin, et al., Science 336 (2012) 893–897.
[36] B. Rungtaweevoranit, J. Baek, J.R. Araujo, et al., Nano Lett. 16 (2016) 7645–7649.
[37] B. An, J. Zhang, K. Cheng, et al., J. Am. Chem. Soc. 139 (2017) 3834–3840.
[38] W. Zhang, L. Wang, K. Wang, et al., Small 7 (2017) 1602583.
[39] Z. Li, T.M. Rayder, L. Luo, J.A. Byers, C.K. Tsung, J. Am. Chem. Soc. 140 (2018) 8082–8085.
[40] W. Zhen, B. Li, G. Lu, J. Ma, Chem. Commun. 51 (2015) 1728–1731.
[41] W. Zhen, F. Gao, B. Tian, et al., J. Catal. 348 (2017) 200–211.
[42] Z.W. Zhao, X. Zhou, Y.N. Liu, et al., Catal. Sci. Technol. 8 (2018) 3160–3165.
[43] F. Guo, Y.P. Wei, S.Q. Wang, et al., J. Mater. Chem. A 7 (2019) 26490–26495.
[44] D. Sun, W. Liu, Y. Fu, et al., Chem. Eur. J. 20 (2014) 4780–4788.
[45] M. Choi, D. Kim, B. Rungtaweevoranit, et al., J. Am. Chem. Soc. 139 (2017) 356–362.
[46] F. Guo, S. Yang, Y. Liu, et al., ACS Catal. 9 (2019) 8464–8470.
[47] C. Li, Y. Wang, F. Yu, X. Shen, C. Duan, J. Mater. Chem. A 7 (2019) 11355–11361.
[48] S.M. Liu, Z. Zhang, X. Li, et al., Adv. Mater. Interfaces 5 (2018) 1801062.
[49] X. Wang, F.M. Wisser, J. Canivet, M. Fontecave, C. Mellot-Draznieks, ChemSusChem 11 (2018) 3315–3322.
[50] Z.H. Yan, B. Ma, S.R. Li, et al., Sci. Bulletin 64 (2019) 976–985.
[51] Z.C. Kong, J.F. Liao, Y.J. Dong, et al., ACS Energy Lett. 3 (2018) 2656–2662.
[52] L.Y. Wu, Y.F. Mu, X.X. Guo, et al., Angew. Chem. Int. Ed. 58 (2019) 9491–9495.
[53] Q. Liu, Y. Zhou, J. Kou, et al., J. Am. Chem. Soc. 132 (2010) 14385–14387.
[54] N. Zhang, S. Ouyang, P. Li, et al., Chem. Commun. 47 (2011) 2041–2043.
[55] J. Zhao, Y. Wang, Y.X. Li, X. Yue, C.Y. Wang, Catal. Sci. Technol. 6 (2016) 7967–7975.
[56] Q. Liu, Z.X. Low, L. Li, et al., J. Mater. Chem. A 1 (2013) 11563–11569.
[57] H. Zhao, X. Wang, J. Feng, et al., Catal. Sci. Technol. 8 (2018) 1288–1295.
[58] K.M. Cho, K.H. Kim, K. Park, et al., ACS Catal. 7 (2017) 7064–7069.
[59] J. Jin, J. Yu, D. Guo, C. Cui, W. Ho, Small 11 (2015) 5262–5271.
[60] C. Chen, T. Wu, H. Wu, et al., Chem. Sci. 9 (2018) 8890–8894.
[61] H. Chen, C.E. Nanayakkara, V.H. Grassian, Chem. Rev. 112 (2012) 5919–5948.
[62] M. Wang, D. Wang, Z. Li, Appl. Catal. B 183 (2016) 47–52.
[63] S. Yan, S. Ouyang, H. Xu, et al., J. Mater. Chem. A 4 (2016) 15126–15133.
[64] X. Chen, J. Zhang, X. Fu, M. Antonietti, X. Wang, J. Am. Chem. Soc. 131 (2009) 11658–11659.
[65] Z. Lin, X. Wang, Angew. Chem. Int. Ed. 52 (2013) 1735–1738.
[66] S. Yang, Y. Gong, J. Zhang, et al., Adv. Mater. 25 (2013) 2452–2456.
[67] P. Niu, L. Zhang, G. Liu, H.M. Cheng, Adv. Funct. Mater. 22 (2012) 4763–4770.
[68] X. Lu, K. Xu, P. Chen, et al., J. Mater. Chem. A 2 (2014) 18924–18928.
[69] L. Shi, T. Wang, H. Zhang, K. Chang, J. Ye, Adv. Funct. Mater. 25 (2015) 5360–5367.
[70] Y. Wang, W. Zhen, Y. Zeng, et al., J. Mater. Chem. A 8 (2020) 6034–6040.
[71] X. Wang, X. Zhao, D. Zhang, G. Li, H. Li, Appl. Catal. B 228 (2018) 47–53.
[72] N. Sadeghi, S. Sharifnia, T.O. Do, J. Mater. Chem. A 6 (2018) 18031–18035.
[73] X. Jiang, H. Wu, S. Chang, et al., J. Mater. Chem. A 5 (2017) 19371–19377.
[74] X. Tian, C. Yu, C. Zhao, et al., ACS Appl. Mater. Interfaces 11 (2019) 9904–9910.
[75] H. Atzkern, B. Huber, F.H. Kohler, G. Müller, R. Müller, Organometallics 10 (1991) 238–244.
[76] Z. Xin, Y.R. Wang, Y. Chen, et al., Nano Energy 67 (2020) 104233.
[77] J.C. Cardoso, S. Stulp, J.F.D. Brito, et al., Appl. Catal. B 225 (2018) 563–573.

Biography of corresponding author

Prof. Li Zhang received her PhD from The Hong Kong University of Science and Technology in 2008. After postdoctoral work at the Scripps Research Institute for 2 years, she has begun her independent career at Sun Yat-Sen University since 2010. Her current research is focused on organometallics and heterogeneous catalysis.